Direct Nanoscale Imaging of Evolving Electric Field Domains in Quantum Structures

Citation: Dhar, Rudra Sankar, Seyed Ghasem Razavipour, Emmanuel Dupont, Chao Xu, Sylvain Laframboise, Zbig Wasilewski, Qing Hu, and Dayan Ban. "Direct Nanoscale Imaging of Evolving Electric Field Domains in Quantum Structures." Sci. Rep. 4 (November 28, 2014): 7183.

As Published: http://dx.doi.org/10.1038/srep07183

Publisher: Nature Publishing Group

Persistent URL: http://hdl.handle.net/1721.1/92590

Version: Final published version: final published article, as it appeared in a journal, conference proceedings, or other formally published context

SCIENTIFIC REPORTS

OPEN

SUBJECT AREAS:
QUANTUM CASCADE LASERS
SCANNING PROBE MICROSCOPY

Received
23 October 2014

Accepted
7 November 2014

Published
28 November 2014

Correspondence and requests for materials should be addressed to D.B. (dban@uwaterloo.ca)

Direct Nanoscale Imaging of Evolving Electric Field Domains in Quantum Structures

Rudra Sankar Dhar[1], Seyed Ghasem Razavipour[1], Emmanuel Dupont[2], Chao Xu[1], Sylvain Laframboise[2], Zbig Wasilewski[1], Qing Hu[3] & Dayan Ban[1]

[1]Department of Electrical and Computer Engineering, Waterloo Institute for Nanotechnology, University of Waterloo, 200 University Ave. West, Waterloo, N2L3G1, Ontario, Canada, [2]National Research Council, Bldg. M-50, 1200 Montreal Rd, Ottawa, Ontario K1A0R6, Canada, [3]Department of Electrical Engineering and Computer Science, Research Laboratory of Electronics, Massachusetts Institute of Technology, Cambridge, Massachusetts, 02139, USA.

The external performance of quantum optoelectronic devices is governed by the spatial profiles of electrons and potentials within the active regions of these devices. For example, in quantum cascade lasers (QCLs), the electric field domain (EFD) hypothesis posits that the potential distribution might be simultaneously spatially nonuniform and temporally unstable. Unfortunately, there exists no prior means of probing the inner potential profile directly. Here we report the nanoscale measured electric potential distribution inside operating QCLs by using scanning voltage microscopy at a cryogenic temperature. We prove that, per the EFD hypothesis, the multi-quantum-well active region is indeed divided into multiple sections having distinctly different electric fields. The electric field across these serially-stacked quantum cascade modules does not continuously increase in proportion to gradual increases in the applied device bias, but rather hops between discrete values that are related to tunneling resonances. We also report the evolution of EFDs, finding that an incremental change in device bias leads to a hopping-style shift in the EFD boundary – the higher electric field domain expands at least one module each step at the expense of the lower field domain within the active region.

Since the inception of terahertz (THz) quantum cascade lasers (QCLs) in 2002[1], the past decade has witnessed momentous progress in the development of compact semiconductor THz coherent sources[2,3,4]. Several THz QCL devices have been demonstrated, based on different quantum active region designs, including chirped superlattice (CSL), bound-to-continuum (BTC), resonant-phonon (RP) and indirect-pumping (IDP) schemes[3,5,6]. Significant effort has been placed on improving device performance, not only through optimized active region design, but also innovative waveguide engineering, high-quality molecular beam epitaxy growth and advanced device fabrication techniques. Lasing frequencies ranging from 1.2 to 5.2 THz[7,8] were measured from THz QCLs in the absence of a magnetic field. Broadband lasing[9] and continuously-tunable lasing[10] of THz QCLs have also been demonstrated. The maximum lasing temperature of THz QCLs has significantly improved[11–16] over the last decade and output power has now reached to 470 mW in pulsed mode[17]. Mode-locked THz QCLs[18], THz QCLs with large wall plug efficiency[19], photonic crystal THz QCLs[20], THz QCLs with low divergence emission beams[21,22] have been realized. More recently, broadly-tunable terahertz generation based on difference frequency generation in the cavity of a mid-infrared quantum cascade laser was reported[23]. The aforementioned rapid advances yield a fairly good understanding of terahertz quantum cascade lasers even though room temperature operation has yet to be achieved[24].

Thus far, fabricated THz QCLs have typically been characterized using conventional electrical and optical techniques, such as pulsed and/or DC light-current-voltage[11,25], lasing spectrum and far-field pattern measurements[26]. The THz time-domain spectroscopy technique was successfully applied to probe actively-biased THz QCLs, enabling direct measurement of the optical gain/loss of the active region[27,28]. The intrinsic linewidth of THz QCLs was also experimentally investigated[29]. By contrast, transmission electron microscopy (TEM) and scanning electron microscopy (SEM) have been employed to obtain static microscopic structure information, such as direct measurement of the interface roughness in QCL materials[30] or visual inspection of QCL laser emission facets[31]. Until recently, THz QCL characterization techniques were limited to either input/output behaviors or static structural information. Internal nanoscopic origins and external macroscopic performance measures were sel-

dom linked through compelling experimental observation. As a result, very little direct evidence has been produced to advance our understanding of why many devices fail or perform poorly. In particular, there was an inability to directly and quantitatively profile electric potentials across quantum cascade modules.

The voltage distribution plays a key role in governing device performance, especially for THz QCLs; it dictates how efficiently electrons are injected into desired states to achieve sufficient population inversion – a prerequisite for lasing. It is therefore critically important to measure the voltage distribution within an actively-driven laser directly. Scanning voltage microscopy (SVM) is a novel and enabling tool to quantitatively probe the voltage distribution and has sufficiently high spatial resolution to even resolve individual quantum wells[32,33,34]. This could disclose important experimental evidence for the formation and evolution of electric field domains in semiconductor quantum structures that are based on electron resonant tunneling, which has long been hypothesized and only verified indirectly through the observation of sawtooth-like current-voltage (I–V) or light-voltage (L–V) curves or the measurements of active-region photoluminescence spectra or cathodoluminescence imaging[35–38].

Conventional SVM has found limited application to lasing THz QCLs because measurements can only be performed at room temperature, while current THz QCLs can only be operated at cryogenic temperatures. Furthermore, many interesting quantum dynamics (such as optical and electrical instability and formation of electric field domains) can only be observed at low temperatures[39]. Rapidly increasing progress in the design and fabrication of THz QCLs with improved performance may help overcome this barrier, for example, THz QCLs that can lase up to ~200 K have already been demonstrated[15]. In addition, cryogenic temperature SVM apparatus that can be operated at liquid helium or liquid nitrogen temperatures with a nanometer resolution have been successfully developed for research utilization, and are readily accessible using modern scanning probe microscope technology.

With the set-up described in the Methods section we have directly measured the voltage profile across the transverse cross section of the active region of a lasing THz QCL at 77 K, resolving individual quantum cascade modules. Knowledge of the electric field distribution profile is essential when studying QCL technologies, in which the energy level alignment across modules plays a critical role in overall device performance. According to the quantum mechanical description of resonant tunneling, the electric current is maximized when the two quantum levels are aligned. Afterwards, the tunneling current begins to drop as the bias further increases – generating a negative differential resistance (NDR) region[40]. Although the active region of a THz QCL typically consists of up to hundreds of nominally-identical cascade modules, most THz QCL device models[41–44] simulate only one cascade module in principle. Such modeling is based on an implicit and important assumption that the electric field is uniform across the entire quantum structures so that each module experiences the same bias condition. It is therefore presumed that the collective current density–voltage (J-V) behavior of the entire active region can be represented by the individual J-V of a single quantum cascade module. In the present detection scheme, we directly and compellingly reveal that the quantum cascade modules in a THz QCL active region could be operating under distinctly different bias conditions (different electric fields), which is observed both below and above the lasing threshold over a wide range of applied device biases.

The device under test is an indirect pumping-based THz QCL laser with uncoated cleaved facets on both ends of a metal-metal waveguide[6]. The two-dimensional voltage profile across the device active region is obtained by scanning a conductive cantilever probe over a transverse cross section area (11×11 μm^2) on the front emission facet as the device is biased at 12 V in pulsed mode at 77 K (Fig. 1a), clearly revealing a monotonically drop in voltage from the top metals (positively biased at 12 V), across the intermediate layers, to the grounded bottom metals (at 0 V). A sharp voltage drop of ~0.7–0.8 V is observed at the Schottky-like junction between the top metal (un-annealed) and the top n^+ GaAs contact layer. No substantial voltage drop is observed at the interface between the bottom metal and the bottom contact layer due to its Ohmic-like contact[6]. Most strikingly, the image visualizes the formation of two electric field domains (EFDs) across the ~10 μm thick active region at this bias, one close to the top metal layer, which has a higher electric field (greater slope), and one close to the bottom metal layer, which has a lower electric field (smaller slope). The inset image shows the topology of the scanned cross section of the cleaved emission facet. Only slight height differences are evident between five layers – the top metal layer, the top n^+ GaAs contact layer, the ~10 μm thick multi-quantum-well active region, the bottom n^+ GaAs contact layer and the bottom metal layer. The topology image confirms that the cross section of the ~10 μm thick multi-quantum-well active region is almost atomically flat.

Similar SVM scans are performed at different applied device biases ranging from 2 V up to 25 V with steps of 2, 1 or 0.5 V. It is worthy of note that the last few bias points exceed the final device NDR, which is at ~21.8 V. By averaging cross-section line scans that make up a two-dimensional (2D) SVM image similar to the one shown in Fig. 1a, one-dimensional SVM measured voltage profile curves are obtained as a function of the distance from the top metal layer (Fig. 1b, c). At low biases (2 V to 9 V), the electric field is almost uniform across the entire active region (one slope) and the slope of the voltage profile curves over the active region increases proportionally with the increase of the applied device bias. Beyond 10 V, however, two slopes start to emerge across the ~10 μm thick active region. As the device bias further increases, the two slopes remain almost unchanged while the boundary between the higher electric field domain (denoted by dashed-lines) and the lower electric field domain (solid-lines) evenly shifts from the top metal layer to the bottom metal layer. At a bias between 17 V and 18 V, the higher EFD expands over the entire active region. At higher biases of 18 V to 21 V, only one slope can be observed in the voltage curves, which increases proportionally to the applied device bias. For device biases between 22 V and 25 V, two slopes again emerge and the higher electric field domain expands from the top metal layer to the bottom metal layer at the expense of the lower electric field domain. The lasing threshold voltage of this device at 77 K is ~20.4 V, so the SVM results show the formation of EFDs not only below but also above the lasing threshold.

One major advantage of SVM is its quantitative analysis – the electric field (F) within the observed EFDs can be exactly quantified from the slopes (F = average of ($\Delta V/\Delta d$)) of the voltage profile curves in Figs. 1b and 1c. The derived results are shown in Table I. Over pre-threshold device biases spanning 10 to 17 V, two distinct electric fields (F_1 and F_2) are observed. At different device biases, F_1 varies slightly from 8.574 to 8.586 kV/cm with an average of 8.58 kV/cm, while F_2 varies from 16.763 to 16.770 kV/cm with an average of 16.77 kV/cm. Two new electric fields (F_3 and F_4) emerge at biases above the lasing threshold, from 22 V to 25 V. At these biases, F_3 and F_4 average 20.96 kV/cm and 24.35 kV/cm, respectively. Note that this marks a direct and quantitative measurement of distinctly different EFDs while the semiconductor quantum laser is in operation, illustrating the great potential for cryogenic temperature SVM techniques to advance THz QCL research and development.

The experimental and theoretical light–current density–voltage (L-J-V) characteristics of the device under test can provide useful insights to understand the SVM measured voltage profiles (Fig. 1d). The simulated current density–electric field (J–F) curve reveals three features associated with resonant tunneling processes. The peak at

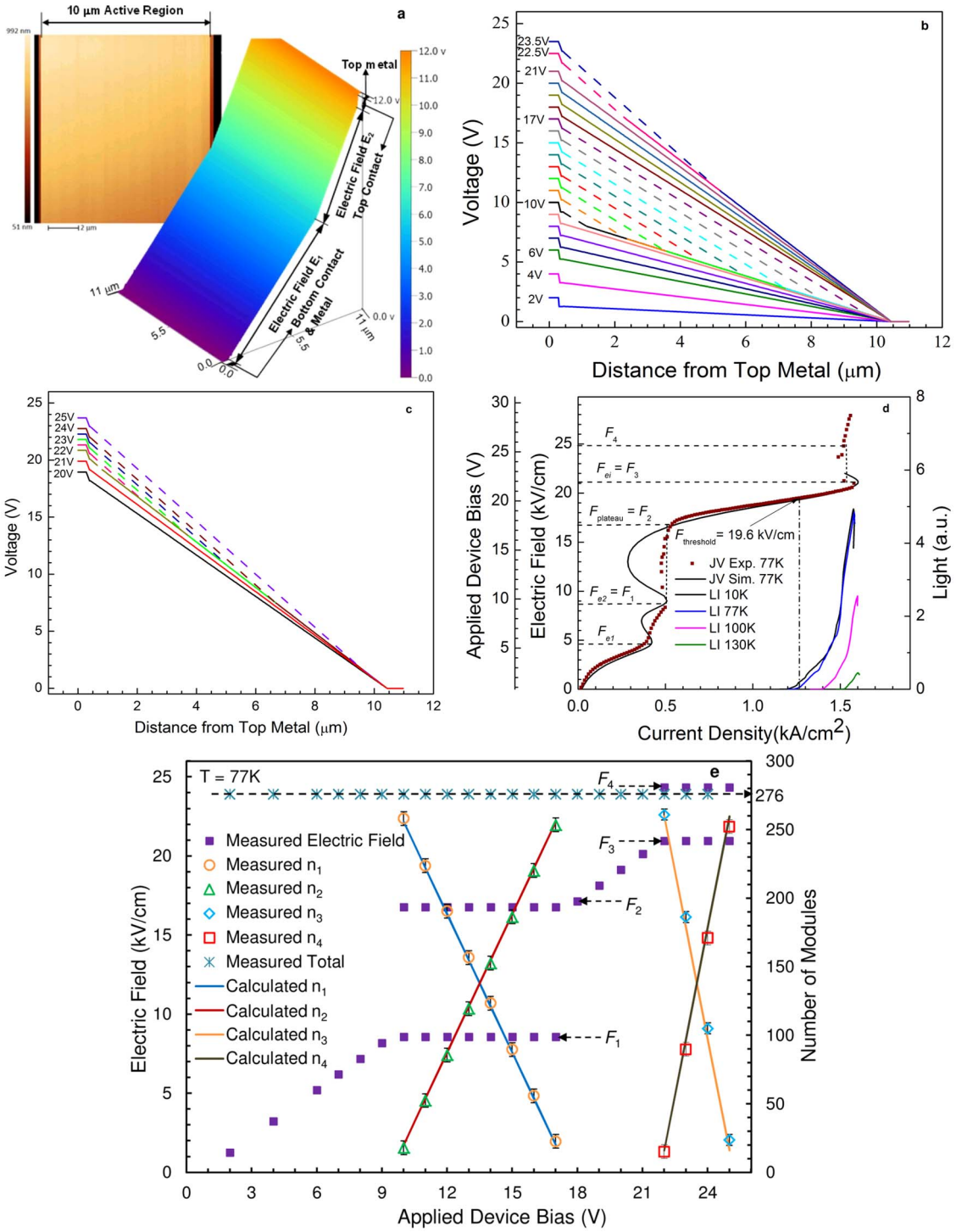

Figure 1 | Formation and evolution of electric field domains in an operating THz QCL. (a), The SVM measured two-dimentional (2D) voltage profile across the active region of a THz QCL (device V843, cooled at 77 K) under a forward bias of 12 V. It shows two electric field domains (F_1 and F_2) across the ~10 μm thick multi-quantum-well active region. The inset of the figure displays a 2D AFM topology image simultaneously acquired over the same area. (b), One dimensional (1D) section analysis of the SVM voltage profile across the active region of the device at applied device biases spanning 2 V–25 V. (c), 1D voltage profile curves at higher biases (20 V to 25 V) with a smaller device bias step (0.5 V) between the SVM scans. The formation and evolution of two electric field domains over the multi-quantum-well active region is clearly observed in device bias ranges spanning 10–17 V and 22–25 V. (d), Experimental current density – device bias (J-V) and simulated current density – nominal active-region electric field (J-F) curves of the V843 device at 77 K, and light – current density (L-J) curves at 77 K and several other temperatures. The threshold electric field is 19.6 kV/cm at 77 K. The nominal active-region electric field is calculated using $(V\text{-}\Phi)/d$, V is the applied device bias, Φ is the Schottky contact drop (~0.8 V) and d is the active region thickness (~10 μm). (e), The SVM measured electric field across individual cascade modules in the active region of operating V843 device as a function of applied device bias. Two EFDs coexist in bias ranges of 10–17 V and 22–25 V. Shown together is the partition number of the cascade modules in each EFD. Discrete symbols (Measured n_k, $k = 1, 2, 3, 4$) are calculated from the first approach ($n_k = l_k/d$) based on the SVM measurment results of EFD length (l_k) in (b and c). Solid lines (Calculated n_k) are calculated from the second approach (see text for details). The sum of the SVM measured module numbers ($n_1 + n_2$, or $n_3 + n_4$) is ~276.

Table I | SVM measured electric field in each observed electric field domain. The electric field values are obtained by linearly fitting the different sections of the voltage curves. The small variation is attributed to small system errors

Applied Device Bias (V)	F_1 (kV/cm)	F_2 (kV/cm)	F_3 (kV/cm)	F_4 (kV/cm)
10.0	8.583	16.767	–	–
11.0	8.574	16.767	–	–
12.0	8.579	16.767	–	–
13.0	8.574	16.763	–	–
14.0	8.586	16.763	–	–
15.0	8.580	16.770	–	–
16.0	8.579	16.770	–	–
17.0	8.583	16.767	–	–
•••	•••	•••	•••	•••
22.0	–	–	20.952	24.347
22.5			20.957	24.347
23.0	–	–	20.961	24.347
23.5			20.955	24.347
24.0	–	–	20.959	24.347
25.0	–	–	20.957	24.347
Average (E_{avg})	**8.58**	**16.77**	**20.96**	**24.35**

around F_{e1} = 4.4 kV/cm is related to the alignment of the extraction state ($e_{m\text{-}1}$) with the lower lasing state (1_m) (see **Supplementary section** for detailed band diagram and wavefunctions). The peak at around F_{e2} = 8.7 kV/cm is related to the alignment of the extraction state ($e_{m\text{-}1}$) with the upper lasing state (2_m), and the peak at around F_{ei} = 21 kV/cm is related to the alignment of the extraction state ($e_{m\text{-}1}$) with the injection state (i_m). The subscript m stands for the index of the modules increasing along the electron flux direction, the subbands in a module are labeled as *e* (for extraction from LLS by resonant phonon scatting) *1*, *2* and *i* (for injection to ULS via resonant phonon scattering). These features are confirmed experimentally and correspond to a shoulder structure at around 4.6 kV/cm, a current plateau starting at around 8.7 kV/cm and a final NDR at around 21 kV/cm in the experimental J-F curve. The experimental curve also shows a turning point at $F_{plateau}$ = ~16.8 kV/cm, where the plateau comes to an end and the current starts to sharply increase. Clearly there is a correlation between these electric fields of resonant tunneling features and those of the high field domains obtained from the SVM measurements, i.e., F_1, F_2 and F_3 quite reasonably match to F_{e2}, $F_{plateau}$ and F_{ei} in quantity, respectively.

This electric field correlation can be understood as follows. When the quantum cascade laser device is biased at ~9.5 V, which corresponds to an electric field of ~8.7 kV/cm across the ~10 μm thick active region after excluding a ~0.8 V Schottky contact drop, all of its 276 cascade modules are uniformly biased at this electric field. The extraction state ($e_{m\text{-}1}$) aligns with the upper lasing state (2_m) of the immediate downstream module, where the current channel due to the *e-2* tunneling resonance is at its peak current-carrying capacity (J_{e2} = ~0.5 kA/cm^2). As the applied device bias continues to increase, the incremental bias would not be evenly distributed among the serially-stacked 276 modules[45]. If it was, the device would experience an NDR due to misalignment of the *e-2* resonance and device current would substantially drop (as shown in the simulation curve of a single module). To accommodate increases in device bias, some of the modules (starting with those closest to the top contact layer, downstream of electron flux) are forced to hop to a higher bias point, switching from the *e-2* to the *e-i* tunneling resonance current channel, which has a higher peak current-carrying capacity. The rest of the cascade modules remain at the *e-2* resonance (F_{e2}), pinning the device current at J_{e2}, which represents the overall current density through all modules in the active region. The exact bias point (electric field) of the switched modules can therefore be determined by drawing a constant current-density line that passes through the peak value of the *e-2* resonance and intersects with the *e-i* resonance curve. This electric field is found to be $F_{plateau}$ = ~16.8 kV/cm (Fig. 1d). Additional increases in device bias are accommodated as more cascade modules switch from the lower bias point (F_{e2}) to the higher bias point ($F_{plateau}$). This trend continues until all cascade modules switch into the *e-i* resonance current channel. This explains why the electric fields of the two observed EFDs are pinned at F_{e2} and $F_{plateau}$, respectively, in the device bias range between 10 and 17 V.

The length (l_k) of each EFD section can be measured directly from the SVM voltage profile curves (Fig. 1b, c). As one cascade module period is d = 36.2 nm[6] in thickness, the number (n_k) of the cascade modules in each EFD section can be obtained from $n_k = l_k/d$ (k = 1, 2). These numbers can also be calculated through a second approach that assumes a linear partition of the cascade modules between the two EFDs (F_1 = 8.58 kV/cm and F_2 = 16.77 kV/cm) that comply with the total applied device bias (V), which yields

$$n_1 + n_2 = 276 \tag{1}$$

$$n_1 F_1 d + n_2 F_2 d + \phi = V, \tag{2}$$

where ϕ is the voltage drop across the Schottky-like junction at the interface of the top metal layer and the top n^+ GaAs contact layer, and V is the applied device bias. The numbers of quantum cascade modules in each EFD are obtained through these two approaches (SVM measured and theoretically calculated), exhibiting very good agreement (Fig. 1e). This confirms that the boundary of the electric field domains linearly shifts from the top to the bottom contact layer (opposite to electron flux direction) as device bias increases.

A similar analysis can be applied to another high field domain transition observed between F_3 and F_4. From the experimental J-F curve taken at 77 K, the device current density reaches its maximum value of J_{NDR} = ~1.6 kA/cm at F_3, corresponding to the alignment of the *e-i* resonance. As the device bias further increases, the current first slightly drops and then bounces back to the value of J_{NDR} at F_4 (see Fig. 1d). F_3 and F_4 thus become observable in the SVM measurements for the same reason F_1 and F_2 do (as described above). However, differences appear in the transition from F_{e1} resonance to F_{e2} resonance (Fig. 1d). The SVM results reveal that the electric field across all cascade modules continuously increases from zero up to F_{e2}, without a standstill at F_{e1}. This could be attributed to the fact that the current density at any intermediate electric field between F_{e1} and F_{e2} might for all time be higher than the peak current density (J_{e1}) of the F_{e1} resonance – considering F_{e1} and F_{e2} are close to each other, it is possible that some broadening mechanisms make their resonant current density peaks broad enough to completely overshadow the valley in between. So the current density through the device can no longer be pinned at J_{e1} when the electric field exceeds F_{e1}. In other

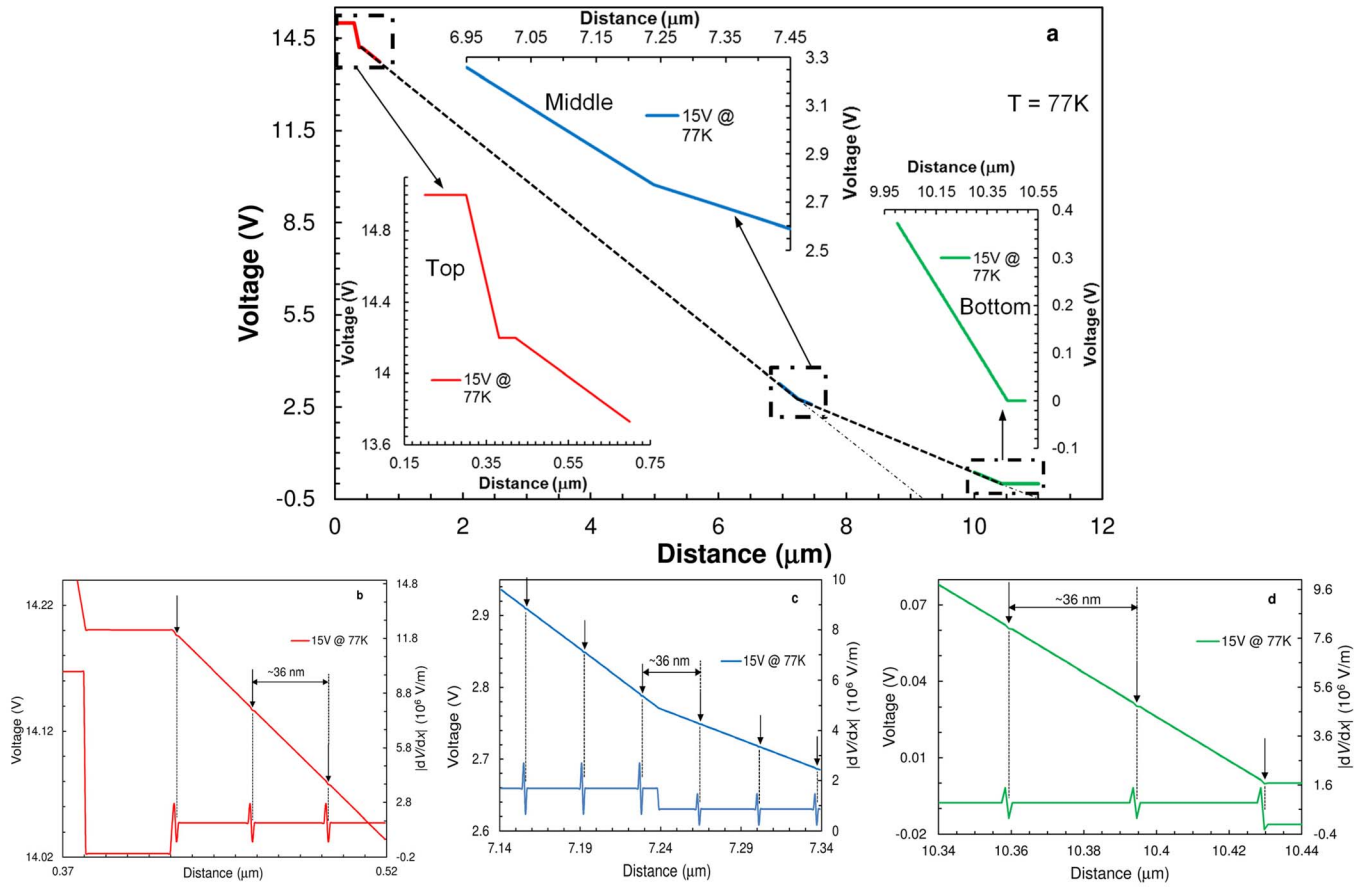

Figure 2 | Rough and high-resolution SVM scans. (a), The 1D SVM voltage curve cross the active region of the V843 device at a bias of 15 V and at T = 77 K. The rough scan (dashed line) spans 11 μm from the top metal layer to the bottom metal layer, clearly showing the co-existence of two electric field domains. It also shows that the voltage curve is straight and smooth in each section. The three zoomed-in scans (one close to the top metal layer, one at the EFD boundary, one close to the bottome metal layer) spans 512 nm each (solid curves in the insets). (b), (c), (d), The corresponding further zoomed-in curves that show the small voltage dips at the delta-doped injection barriers. The bottom curve in each figure (b, c, d) is the first order derivative ($|dV/dx|$) of each corresponding voltage profile curve, for the purpose of identifying the exact location of the voltage dips.

words, the device does not experience a NDR region between F_{e1} and F_{e2}, which is different from results predicted by the theoretical model as shown in Fig. 1d. One possible reason for this discrepancy could be that the broadening due to impurity scattering is likely underestimated in the model. Nevertheless, the experimental curve indeed shows that only a shoulder feature (instead of a current plateau similar to the one between F_{e2} and F_{plateau}) is observed at F_{e1}. Hence, no cascade modules are pinned at F_{e1} and an EFD does not emerge at F_{e1} in the SVM measurements. Only one uniform electric field domain is observed over the device bias range between 2 V and 9 V, in which the electric field increases proportionately with the device bias. The same behavior is observed over the device bias range from 18 to 21 V, where the device current again increases monotonically with the device bias. Looking at the SVM-measured electric field across individual cascade modules as a function of applied device bias, one can clearly notice two gaps, over which the electric field hops directly from F_1 to F_2 and from F_3 to F_4, respectively (Fig. 1e). The SVM measurements also clearly and quantitatively resolve the voltage drop across the Schottky-like junction at the top metal/semiconductor interface (Fig. 1b, 1c), the depletion region of which is mainly in the semiconductor side[46]. The voltage drop across this Schottky-like junction ranges from 0.723 V to 0.812 V at biases of 2 to 25 V (see **Supplementary section**), confirming the hypothesis put forward in previous publications that predict a 0.8 V Schottky contact drop[6,39,47].

Individual quantum cascade modules can be resolved in high-resolution SVM scans by reducing the scan range. In a one-dimensional (1D) rough SVM scan at a device bias of 15 V, the measured voltage profile exhibits two distinct sections over the ~10 μm multi-quantum-well active region and the curve in each section appears smooth and straight (Fig. 2a). By zooming in the SVM scans in three 512 × 512 nm^2 regions – one close to the top metal/semiconductor interface, one close to the EFD boundary and one close to the bottom metal/semiconductor interface (insets of Fig. 2a) – it is revealed that every ~36 nm in the multi-quantum-well active region a small voltage dip can be observed in zoomed-in 1D voltage profile curves (Fig. 2b, c, d). This small voltage dip (~1.2 mV) can be attributed to the delta-doping profile ($\eta_{2D} = 3.25 \times 10^{10}$ cm^{-2}) in the injection barrier, which is the first layer of each cascade module from the upstream of the electron flux as well as the boundary layer between two neighboring modules. A back-of-the-envelope estimation indicates, at most, an additional potential drop between the upstream state e and the delta doping of ~5 mV. The origin of the sharp dip in potential at such a low doping level is not understood yet – maybe due to some very localized oxidation – and will be the subject of further studies. Nevertheless, by high resolution SVM scans in the proximity of the top and bottom contacts we are certain the positions of the voltage dips correspond to the nominal coordinates of delta-doping (Sup Mat figure S7). This particularity is very helpful in this study and is used as a "ruler".

The high-resolution SVM scans over the 512 × 512 nm^2 region that is close to the EFD boundary region identifies the exact location of the EFD boundary and reveals how it evolves (Fig. 3). Two voltage slopes can easily be distinguished over a span of 14 cascade modules –

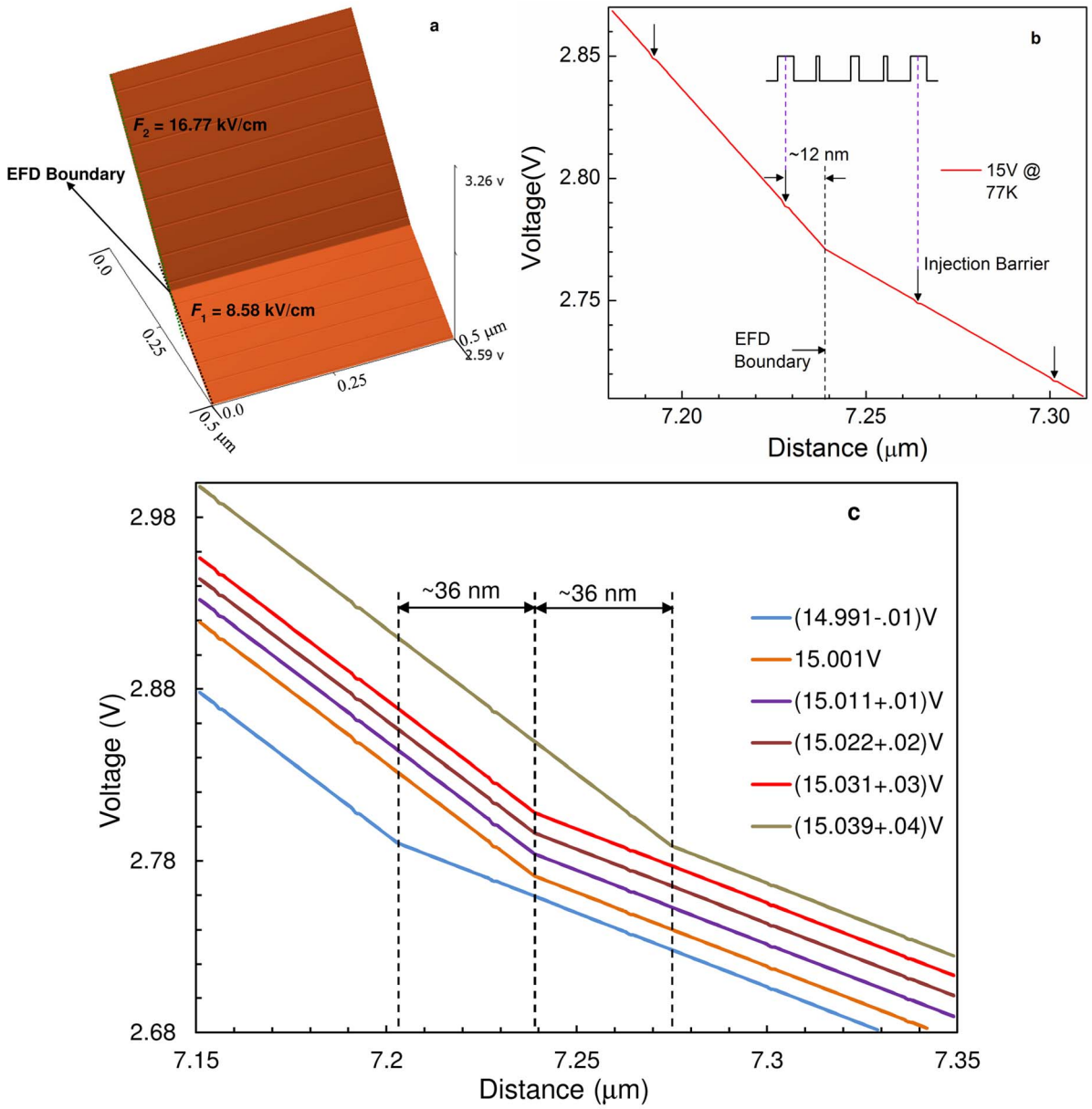

Figure 3 | Resolution of individual quantum cascade modules and the boundary of EFDs. (a), The 2D SVM voltage image over a 512 × 512 nm^2 scan area near the EFD boundary on the V843 device at 15 V and 77 K. It clearly reveals two electric fields over a span of 14 cascade modules. The period of each individual cascade module is measured from the figure to be ~36.1 ± 0.1 nm. (b), A 1D zoomed-in view of three consecutive modules near the EFD boundary. The the EFD boundary, in other words the turning point of the electric field, locates at ~12 nm ± 0.5 nm to the upstream of the delta-doped injection barrier layer of one module. (c), 1D SVM votlage profile curves at a series of device biases with a small incremental bias step (~10 ± 1 mV increase each time). The EFD boundary does not shift if the device bias increase is less than ~30 mV. When it does, the EFD boundary hops at least one module each time (a phenomenon we term *EFD boundary hopping*). All curves (except the one at 15.001 V) are accumulatively shifted by 0.01 V vertically for clarity.

the boundary of each module is denoted by lines of small voltage dip (Fig. 3a). The periodic spacing is measured from zoomed-in high-resolution scans to be ~36.1 ± 0.1 nm, in excellent agreement with the design value of 36.2 nm (0.3% relative error). Each cascade module consists of four GaAs quantum wells (6.1 to 8.5 nm in thickness) and four $Al_{0.25}Ga_{0.75}As$ barrier layers (0.9 to 4.4 nm), they are not individually distinguishable in SVM measurements because of very small (or even zero) voltage contrast at the interfaces between the wells and the barriers except the small voltage dip at the delta-doped injection barrier. By further zooming the SVM scan into only three modules, the EFD boundary is evidently disclosed to locate at ~12 nm ± 0.5 nm away from the small voltage dip (the injection barrier) towards the upstream direction of the electron flux (Fig. 3b), where electrons typically piles up on the extraction (*e*) state before tunneling to the injection state (*i*) of the downstream module. The electric field discontinuity across the EFD boundary is attributed to charge imbalance in the transition region, which is resulted from this electron accumulation on the *e* state. The associated electron sheet density (η_e) can be estimated by Gauss' law, yielding

$$q(\eta_e - \eta_{2D}) = \varepsilon_0 \varepsilon_r (F_2 - F_1) \quad (3)$$

where ε_0 is the vacuum permittivity, ε_r the relative permittivity of GaAs (12.5 at 80 K), F_1 = 8.58 kV/cm, F_2 = 16.77 kV/cm, q electron charge (1.6 × 10^{-19} C) and η_{2D} = 3.25 × 10^{10} cm^{-2}, which is the nominal dopant sheet density in the injection barrier.

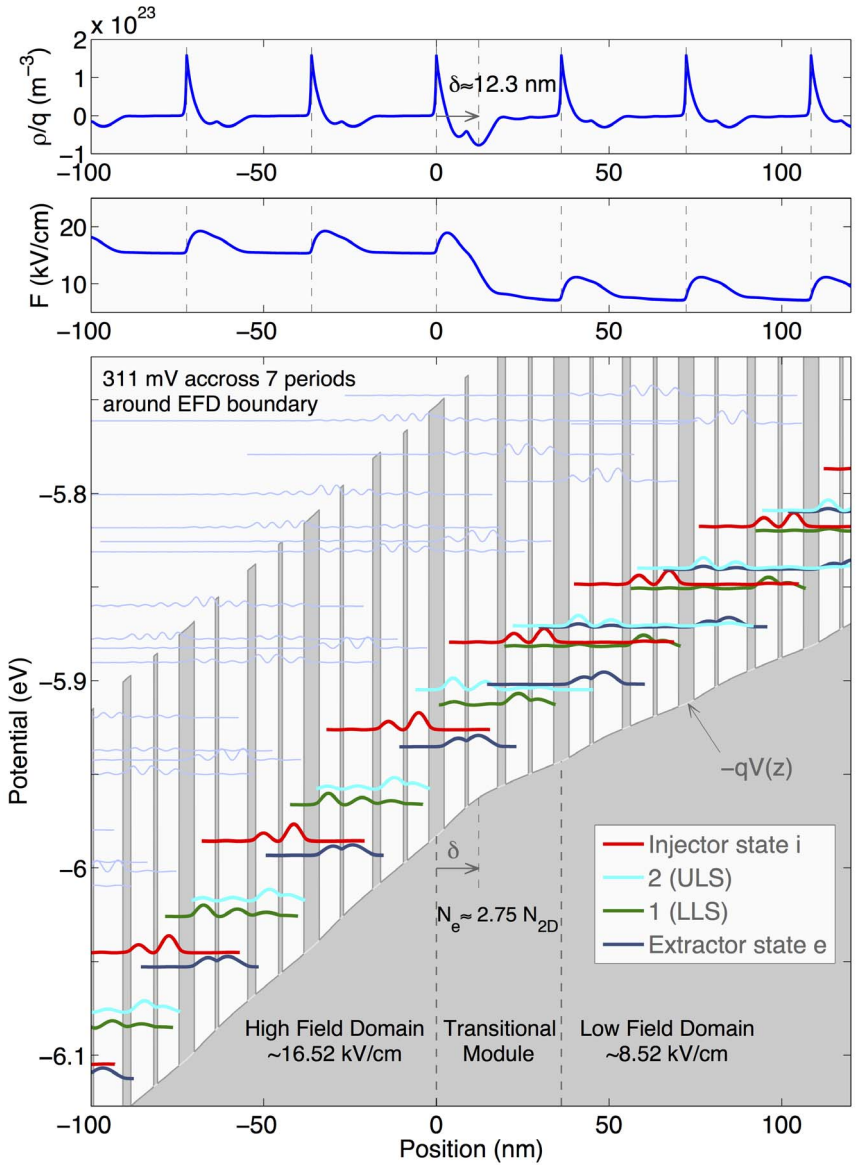

Figure 4 | Simulation of the EFD boundary. Self-consistently solving the coupled Schrödinger-Poisson equations yields the simulation results of electron wavefunction and band diagram across the EFD boundary, confirming the EFD boundary is ~12.3 nm away from the delta-doped injection barrier in the transitional module. The delta-doped dopants are assumed to exponentially diffuse (by 48 Ang/decade) to the upstream direction of electron flux due to Si segregation during the molecular beam epitaxy of the QCL structure. The line running at GaAs conduction band edge (in gray and white) is the potential curve $V(z)$ that the SVM tries to measure. The two curves on the top show the simulated charge density profile and electric field profile, respectively. The simulation is performed at a device bias of 12 V.

The calculation yields $\eta_e = 8.92 \times 10^{10}$ cm^{-2}. Note that this is roughly 2.74 times the nominal dopant sheet density in one module.

Because the EFD boundary is associated with charge accumulation, it has to coincide with a quantum well (or wells) in which the presence of electron wavefunction is substantial (i.e., the extraction state in this case). This implies that the EFD boundary doesn't shift continuously with the gradual increase of the applied device bias, but rather hops discretely and chaotically, which is confirmed in a series of SVM scans with a much smaller incremental step (~10 mV each time) in the applied device bias (Fig. 3c). At a device bias of 14.991 ± 0.001 V, the EFD boundary locates at ~7.203 ± 0.0005 μm. When the device bias increases to 15.001 ± 0.001 V, the EFD boundary jumps to ~7.239 ± 0.0005 μm and remains unchanged at next three biases of 15.011 ± 0.001, 15.022 ± 0.001, and 15.031 ± 0.001 V. When the device bias further increases to 15.039 ± 0.001 V, the EFD boundary jumps again to ~7.275 ± 0.0005 μm. The EFD boundary hops each time by a distance of ~36 ± 0.5 nm, which is exactly the thickness of one module. Apparently, the EFD boundary would not shift if the accumulative increases of the applied device bias are smaller than (16.77 kV/cm–8.58 kV/cm) × 36 nm = ~30 mV, which is the minimum bias increase needed to switch one module from the lower EFD (F_1) to the higher EFD (F_2). This one-module-at-a-time progression of the EFD boundary is therefore convincingly confirmed to be the nanoscopic origin of the reported sawtooth-like current-voltage (I–V) characteristics exhibited by QCLs[48]. If the curves were not vertically shifted in Fig. 3c, the potential curves in the lower field domain would overlay almost perfectly on top of each other whereas the potential curves in the high field domain are clearly spaced by ~10 mV at the end of the last module (m = 276). This means that during a $\lesssim$ 30 mV increase of applied bias between two hopping events the additional potential is mainly distributed in the

higher field domain, i.e., the electric field "flexes" in the higher field domain before going back to its "rest" value when the EFD boundary has just shifted by one module.

Quantum cascade modules in the close proximity of the EFD boundary are simulated by self-consistently solving coupled Schrödinger-Poisson equations. The lower electric field (F_1), the higher electric field (F_2) and the voltage drop across seven modules around the EFD boundary, which are derived from a high-resolution SVM scan at 12 V – are employed as input parameters in the simulation. For the sake of simplicity, carriers are assumed at thermal equilibrium (100 K) in each module. The band diagram and the potential profile across the modules are calculated. The simulation results confirm that the transition from the lower electric field domain to the higher electric field domain occurs inside one cascade module, with a fairly-resolvable turning point (Fig. 4). The turning point of the potential profile coincides with the lobe of the wavefunction of the extraction state (e) in the widest well of the lower phonon stream, which is ~12.3 nm away from the center of the injection barrier layer. It is worthy to note that the first- and second-order derivatives of the potential profile yield electric field profile and charge density profile, respectively. Electron accumulation is indeed observed at the EFD boundary in the simulation curve.

As expected, in the low field domain (the right side in the figure) the levels e_{m+1} and 2_m are almost perfectly anti-crossed (coupling strength $\Omega_{e2} = 0.24$ meV), and in the high field domain (the left side) e_m and i_{m+1} start to be coupled, resulting in a positive differential conductivity of this domain (Fig. 4). We recall that the subscript m stands for the index of the modules increasing from right to left. Across the downstream injection barrier of the transitional module (in which the EFD boundary is located) the levels e_m and 2_{m+1} are fairly detuned and levels e_m and i_{m+1} are still weakly coupled, which puts this short section in negative differential conductivity region and commands extra charge accumulation in e_m to maintain current conservation through this transitional module. Similar argument could be applicable to the levels e_{m-1} and 2_m who just passes their anti-crossing according to the simulation. The impact of the electric field domain boundary on the transport behavior of THz QCLs is profound. The transitional cascade module across the EFD boundary is divided into two sections with different electric fields, so its energy levels are not well aligned. As a result, electron transport across the EFD boundary is nonresonant and may limit the current[37]. Advances in hybrid electron transport, which combines resonant and nonresonant tunneling to support efficient transport in semiconductor quantum systems such as THz QCLs with multiple EFDs are of great interest and crucial importance. However, additional experimental and theoretical work is needed to fully understand these mechanisms.

New ability to probe quantum photonic devices while in operation and on a nano-scale will open critical new avenues of experimental analysis and enable direct measurement of many fundamental physical parameters. In this way, the nanoscopic origins and macroscopic functions will be compellingly connected. The underlying mechanisms responsible for device failures and sub-par performance will be identified with certainty, which will not only facilitate, but accelerate device design and optimization processes. The cryogenic temperature SVM and other associated techniques[32,33,34,49–53] can be employed to measure important inner workings such as the device's voltage profile, dopant profile, charge carrier profile and current profile at nanometric scales and in two dimensions. It will also allow us to visualize the development and evolution of high electric field domains in not only THz QCLs, but also semiconductor superlattices and other resonant-tunneling based quantum structures, to study the extra voltage drop across THz QCLs without the top n^+ GaAs contact layer, and to examine whether the electron injection from the bulk contact layer into the first quantum cascade module is well aligned as expected. If the spatial resolution and voltage sensitivity are further improved, this technique may reveal subtle information such as electron cloud distribution inside a module – the observation of which would shed light into thermal backfilling issues. The technique may also help to understand how the stimulated emission reconfigures the electric field inside a module as the radiative wells should become more conductive upon the ignition of stimulated emission. The technique we have presented is not limited to QCLs, but is applicable to many other active quantum devices and nanoelectronics, such as quantum-well infrared photodetectors (QWIP), semiconductor quantum-well optical amplifiers, semiconductor modulators, single electron transistors, spintronic devices, oscillators based on resonant tunneling and Gunn effect, to name but a few. The domain boundary in our measured QCLs looks stable with a sharp transition from one domain to another but the SVM technique could be able to probe domain instability in weakly-coupled semiconductor superlattices[54] at nanometer scales, which so far have been attracting extensive research interests[55–59].

Methods

We use a cryogenic-temperature conductive atomic force microscope (AFM) to conduct all of the scanning voltage microscopy (SVM) measurements. After mounting the THz QCL device under test, the whole AFM microscope head is cooled to 77 K by submerging it in a chamber filled with liquid nitrogen. A diamond-coated Boron-doped AFM cantilever probe is employed to access the electric signal from the actively-biased THz QCL device in the scans (See **Supplementary section**). The conductive AFM probe scans the laser devices in contact mode on the cleaved emission facet (uncoated). Detected voltage signals from the AFM cantilever probe are directly fed back into the AFM acquisition system and recorded. The topology of the scanned surface is acquired simultaneously. The measurements are performed on a GaAs/AlGaAs THz-QCL with an indirect pumping scheme (phonon-photonphonon) designed for 3.2 THz (Ref. 6). The THz QCL is biased in pulsed mode, with a pulse width of 3.5 μs and a repetition rate of 100 Hz. Details of the experimental techniques used and the design of the THz-QCL are given in the Methods and Supplementary Information section.

1. Kohler, R. *et al.* Terahertz semiconductor-heterostructure laser. *Nature* **417**, 156–159; DOI: 10.1038/417156a (2002).
2. Scalari, G. *et al.* THz and sub-THz quantum cascade lasers. *Laser Photon. Rev.* **3**, 45–66; DOI: 10.1002/lpor.200810030 (2009).
3. Williams, B. S. Terahertz quantum-cascade lasers. *Nature Photon.* **1**, 517-525; DOI: 10.1038/nphoton.2007.166 (2007).
4. Sirtori, C., Barbieri, S. & Colombelli, R. Wave engineering with THz quantum cascade lasers. *Nature Photon.* **7**, 691-701; DOI: 10.1038/nphoton.2013.208 (2013).
5. Kubis, T., Mehrotra, S. R. & Klimeck, G. Design concepts of terahertz quantum cascade lasers: Proposal for terahertz laser efficiency improvements. *Appl. Phys. Lett.* **97**, 261106; DOI: 10.1063/1.3524197 (2010).
6. Dupont, E. *et al.* A phonon scattering assisted injection and extraction based terahertz quantum cascade laser. *J. Appl. Phys.* **111**, 073111; DOI: 10.1063/1.3702571 (2012).
7. Walther, C. *et al.* Quantum cascade lasers operating from 1.2 to 1.6 THz. *Appl. Phys. Lett.* **91**, 131122; DOI: 10.1063/1.2793177 (2007).
8. Chan, C. W. I., Hu, Q. & Reno, J. L. Ground state terahertz quantum cascade lasers. *Appl. Phys. Lett.* **101**, 151108; DOI; 10.1063/1.4759043 (2012).
9. Scalari, G. *et al.* Broadband THz lasing from a photon-phonon quantum cascade structure. *Opt. Express* **8**, 8043–8052; DOI: 10.1364/OE.18.008043 (2010).
10. Qin, Q., Williams, B. S., Kumar, S., Reno, J. L. & Hu, Q. Tuning a terahertz wire laser. *Nature Photon.* **3**, 732–737; DOI: 10.1038/nphoton.2009.218 (2009).
11. Williams, B. S., Kumar, S., Hu, Q. & Reno, J. L. Operation of terahertz quantum-cascade lasers at 164 K in pulsed mode and at 117 K in continuous-wave mode. *Opt. Express* **13**, 3331–3339; DOI: 10.1364/OPEX.13.003331 (2005).
12. Luo, H. *et al.* Terahertz quantum-cascade lasers based on a three-well active module. *Appl. Phys. Lett.* **90**, 041112; DOI: 10.1063/1.2437071 (2007).
13. Belkin, M. A., *et al.* Terahertz quantum cascade lasers with copper metal-metal waveguides operating up to 178 K. *Opt. Express* **16**, 3242-3248; DOI: 10.1364/OE.16.003242 (2008).
14. Kumar, S., Hu, Q. & Reno, J. L. 186 K operation of terahertz quantum cascade lasers based on a diagonal design. *Appl. Phys. Lett.* **94**, 131105; DOI: 10.1063/1.3114418 (2009).
15. Fathololoumi, S. *et al.* Terahertz quantum cascade lasers operating up to ~200 K with optimized oscillator strength and improved injection tunneling. *Opt. Express* **20**, 3866-3876; DOI: 10.1364/OE.20.003866 (2012).
16. Wade, A. *et al.* Magnetic-field-assisted terahertz quantum cascade laser operating up to 225 K. *Nature Photon.* **3**, 41–45; DOI: 10.1038/nphoton.2008.251 (2009).

17. Brandstetter, M. *et al.* High power terahertz quantum cascade lasers with wafer-bonded symmetric active regions. *Appl. Phys. Lett.* **103**, 171113; DOI: 10.1063/1.4826943 (2013).
18. Freeman, J. R. *et al.* Direct intensity sampling of a mode locked terahertz quantum cascade laser. *Appl. Phys. Lett.* **101**, 181115; DOI: 10.1063/1.4765660 (2012).
19. Vitiello, M. S., Scamarcio, G., Spagnolo, V., Dhillon, S. S. & Sirtori, C. Terahertz quantum cascade lasers with large wall-plug efficiency. *Appl. Phys. Lett.* **90**, 191115; DOI: 10.1063/1.2737129 (2007).
20. Chassagneux, Y. *et al.* Electrically pumped photonic-crystal terahertz lasers controlled by boundary conditions. *Nature* **457**, 174–178; DOI: 10.1038/nature07636 (2009).
21. Amanti, M. I., Fischer, M., Scalari, G., Beck, M. & Faist, J. Low-divergence single-mode terahertz quantum cascade laser. *Nature Photon.* **3**, 586–590; DOI: 10.1038/nphoton.2009.168 (2009).
22. Yu, N. *et al.* Small-divergence semiconductor lasers by plasmonic collimation. *Nature Photon.* **2**, 564-570; DOI: 10.1038/nphoton.2008.152 (2008).
23. Vijayraghavan, K. *et al.* Broadly tunable terahertz generation in mid-infrared quantum cascade lasers. *Nature Commun.* **4**, 2021; DOI: 10.1038/ncomms3021 (2013).
24. Kumar, S., Chan, C. W. I., Hu, Q. & Reno, J. L. A 1.8-THz quantum cascade laser operating significantly above the temperature of $\hbar\omega$/kB. *Nature Phys.* **7**, 166–171; DOI: 10.1038/nphys1846 (2011).
25. Fathololoumi, S. *et al.* Time resolved thermal quenching of THz quantum cascade lasers. *IEEE J. Quantum Electron.* **46**, 396-404; DOI: 10.1109/JQE.2009.2031250 (2010).
26. Fathololoumi, S. *et al.* Electrically switching transverse modes in high power THz quantum cascade lasers. *Opt. Express* **18**, 10036-10048; DOI:10.1364/OE.18.010036 (2010).
27. Kröll, J. *et al.* Phase-resolved measurements of stimulated emission in a laser. *Nature* **449**, 698; DOI: 10.1038/nature06208 (2007).
28. Burghoff, D. *et al.* A terahertz pulse emitter monolithically-integrated with a quantum cascade laser. *Appl. Phys. Lett.* **98**, 061112; DOI: 10.1063/1.3553021 (2011).
29. Vitiello, M. S. *et al.* Quantum-limited frequency fluctuations in a terahertz laser. *Nature Photon.* **6**, 525–528; DOI: 10.1038/nphoton.2012.145 (2012).
30. Lopez, F., Wood, M. R., Weimer, M., Gmachl, C. F. & Caneau, C. G. Direct Measurement of Interface Roughness in QCL Materials Grown by MOCVD. *The 12th International Conference on Intersubband Transitions in Quantum Wells, Sept. 16 – 20th, 2013, Sagamore Resort, Lake George, Bolton Landing, New York. Conference Program*, pages 57-58.
31. Brandstetter, M. *et al.* Influence of the facet type on the performance of terahertz quantum cascade lasers with double-metal waveguides. *Appl. Phys. Lett.* **102**, 231121; DOI: 10.1063/1.4811124 (2013).
32. Ban, D. *et al.* Direct Imaging of the Depletion Region of an InP pn Junction Under Bias Using Scanning Voltage Microscopy. *Appl. Phys. Lett.* **81**, 5057-5059; DOI: 10.1063/1.1528277 (2002).
33. Ban, D. *et al.* Scanning Voltage Microscopy on Active Semiconductor Lasers: the Impact of doping profile near an epitaxial growth interface on Series Resistance. *IEEE J. Quantum Electron.* **40**, 651–655; DOI: 10.1109/JQE.2004.828262 (2004).
34. Ban, D. *et al.* Scanning Voltage Microscopy on Buried Heterostructure Multi-Quantum-Well Lasers: Identification of a Diode Current Leakage Path. *IEEE J. Quantum Electron.* **40**, 118–122; DOI: 10.1109/JQE.2003.821539 (2004).
35. Choi, K. K., Levine, B. F., Malik, R. J., Walker, J. & Bethea, C. G. Periodic negative conductance by sequential resonant tunneling through an expanding high-field superlattice domain. *Phys. Rev. B* **35**, 4172–4175; DOI: 10.1103/PhysRevB.35.4172 (1987).
36. Grahn, H. T., Schneider, H. & Klitzing, K. V. Optical detection of high field domains in GaAs/AlAs superlattices. *Appl. Phys. Lett.* **54**, 1757–1759; DOI: 101063/1.101282 (1989).
37. Grahn, H. T., Haug, R. J., Muller, W. & Ploog, K. Electric-field domains in semiconductor superlattices: A novel System for tunneling between 2D Systems. *Phys. Rev. Lett.* **67**, 1618–1621; DOI: 10.1103/PhysRevLett.67.1618 (1991).
38. Kwok, S. H. *et al.* Cathodoluminescence imaging of electric-field domains in semiconductor superlattices. *Solid-State Electron.* **40**, 527–530; DOI: 10.1016/0038-1101(95)00283-9 (1996).
39. Fathololoumi, S. *et al.* Effect of Oscillator Strength and Intermediate Resonance on the Performance of Resonant Phonon-based Terahertz Quantum Cascade Lasers. *J. Appl. Phys.* **113**, 113109; DOI: 10.1063/1.4795614 (2013).
40. Chang, L. L., Esaki, L. & Tsu, R. Resonant Tunneling in Semiconductor Double Barriers. *Appl. Phys. Lett.* **24**, 593; DOI: 10.1063/1.1655067 (1974).
41. Terrazi, R. & Faist, J. A density matrix model of transport and radiation in quantum cascade lasers. *New J. Phys.* **12**, 033045; DOI: 10.1088/1367-2630/12/3/033045 (2010).
42. Lee, S. C. & Wacker, A. Nonequilibrium Greens function theory for transport and gain properties of quantum cascade structures. *Phys. Rev. B* **66**, 245314; DOI: 10.1103/PhysRevB.66.245314 (2002).
43. Jirauschek, C. & Lugli, P. Monte-Carlo-based spectral gain analysis for terahertz quantum cascade lasers. *J. Appl. Phys.* **105**, 123102; DOI: 10.1063/1.3147943 (2009).
44. Han, Y. J., Feng, W. & Cao, J. C. Optimization of radiative recombination in terahertz quantum cascade lasers for high temperature operation. *J. Appl. Phys.* **111**, 113111; DOI: 10.1063/1.4729531 (2012).
45. Grahn, H. T., Schneider, H. & Klitzing, K. V. Optical studies of electric field domains in GaAs-$Al_xGa_{1-x}As$ superlattices. *Phys. Rev. B* **41**, 2890–2899; DOI: 10.1103/PhysRevB.41.2890 (1990).
46. Chuang, S. L. *Physics of Photonic Devices, Wiley, second edition,* 2009.
47. Razavipour, S. G. *et al.* An indirectly pumped Terahertz Quantum Cascade Laser with low injection coupling strength operating above 150 K. *J. Appl. Phys.* **113**, 203107; DOI: 10.1063/1.4807580 (2013).
48. Wienold, M., Schrottke, L., Giehler, M., Hey, R. & Grahn, H. T. Nonlinear transport in quantum-cascade lasers: The role of electric-field domain formation for the laser characteristics. *J. Appl. Phys.* **109**, 073112; DOI: 10.1063/1.3573504 (2011).
49. Ban, D., Sargent, E. H. & Dixon-Warren, St. J. Scanning Differential Spreading Resistance Microscopy on an Actively Driven Buried Heterostructure Multi-Quantum-Well Laser. *IEEE J. Quantum Electron.* **40**, 865–870; DOI: 10.1109/JQE.2004.830174 (2004).
50. Kuntze, S. B. *et al.* Nanoscopic Electric Potential Probing: Influence of Probe-Sample Interface on Spatial Resolution. *Appl. Phys. Lett.* **84**, 601–603; DOI: 10.1063/1.1643534 (2004).
51. Ban, D. *et al.* Direct Observation of Lateral Current Spreading in Ridge-Waveguide Lasers Using Scanning Voltage Microscopy. *Appl. Phys. Lett.* **82**, 4166–4168; DOI: 10.1063/1.1581982 (2003).
52. Ban, D. *et al.* Two-Dimensional Profiling of Carriers in a Buried Heterostructure Multi-Quantum-Well Laser: Calibrated Scanning Spreading Resistance Microscopy and Scanning Capacitance Microscopy. *J. Vac. Sci. Technol. B* **20**, 2126–2132; DOI: 10.1116/1.1511211 (2002).
53. Ban, D. *et al.* Two-Dimensional Transverse Cross-Section Nanopotentiometry of Actively-Driven Buried Heterostructure Multiple-Quantum-Well Lasers. *J. Vac. Sci. Technol. B* **20**, 2401–2407; DOI: 10.1116/1.1524150 (2002).
54. Rasulova, G. K., Brunkov, P. N., Egorov, A. Yu. & Zhukov, A. E. Self-oscillations in weakly coupled GaAs/AlGaAs superlattices at 77.3 K. *J. Appl. Phys.* **105**, 033711; DOI: 10.1063/1.3072697 (2009).
55. Wacker, A., Moscoso, M., Kindelan, M. & Bonilla, L. L. Current-voltage characteristic and stability in resonant-tunneling *n*-doped semiconductor superlattices. *Phys. Rev. B* **55**, 2466–2475; DOI: 10.1103/PhysRevB.55.2466 (1997).
56. Bonilla, L. L., Galan, J., Guesta, J. A., Martinez, F. C. & Molera, J. M. Dynamics of electric-field domains and oscillations of the photocurrent in a simple superlattice model. *Phys. Rev. B* **50**, 8644–8657; DOI: 10.1103/PhysRevB.50.8644 (1994).
57. Bonilla, L. L. & Grahn, H. T. Non-linear dynamics of semiconductor superlattices. *Rep. Prog. Phys.* **68**, 577–683; DOI: 10.1088/0034-4885/68/3/R03 (2005).
58. Bomze, Yu., Hey, R., Grahn, H. T. & Teitsworth, S. W. Noise-induced current switching in semiconductor superlattices: observation of nonexponential kinetics in a high-dimensional system. *Phys. Rev. Lett.* **109**, 026801; DOI: 10.1103/PhysRevLett.109.026801 (2012).
59. Huang, Y. *et al.* Spontaneous quasi-periodic current self-oscillations in a weakly coupled GaAs/(Al,Ga)As superlattice at room temperature. *Appl. Phys. Lett.* **102**, 242107; DOI: 10.1063/1.4811358 (2013).

Acknowledgments

We acknowledge financial support from Natural Science and Engineering Research Council (NSERC) of Canada, Canadian Foundation of Innovation (CFI), the CMC Microsystems, and Ontario Research Fund (ORF).

Author contributions

R.S.D. set up and conducted SVM experiments, analysed the data and prepared most of the figures. S.G.R. conducted simulations, prepared simulation figures and contributed to experiments and data analysis. E.D. designed the THz QCL device, contributed to some experimental data and analysis and one figure, C.X. contributed to some experimental measurements and data analysis. S.L. fabricated the THz QCL device, Z.W. grew the THz QCL wafer, D.B. and Q.H. initiated the study, Q.H. also contributed samples and suggested improvements to the manuscript. D.B. planned and coordinated the study, contributed to data analysis, prepared a few figures and wrote the manuscript. All authors discussed the results and contributed to the manuscript at various stages.

Additional information

Supplementary Information accompanies this paper at http://www.nature.com/scientificreports

Competing financial interests: The authors declare no competing financial interests.

How to cite this article: Dhar, R.S. *et al.* Direct Nanoscale Imaging of Evolving Electric Field Domains in Quantum Structures. *Sci. Rep.* **4**, 7183; DOI:10.1038/srep07183 (2014).